Available online at www.sciencedirect.com

SciVerse ScienceDirect

Ceramics International 38 (2012) 6253–6266

CERAMICS INTERNATIONAL

www.elsevier.com/locate/ceramint

Anodic TiO_2 Nanotube Arrays for Dye-Sensitized Solar Cells Characterized by Electrochemical Impedance Spectroscopy

Hui Ping Wu[a], Lu Lin Li[a], Chien Chon Chen[b,*], Eric Wei Guang Diau[a,**]

[a]*Department of Applied Chemistry, National Chiao Tung University, Hsinchu 30010, Taiwan*
[b]*Department of Energy Engineering, National United University, Miaoli 36003, Taiwan*

Received 18 January 2012; received in revised form 26 April 2012; accepted 26 April 2012
Available online 23 May 2012

Abstract

This paper reports on the microstructure of anodic titanium oxide (TiO_2) and its use in a dye-sensitized solar cell (DSSC) device. When voltages of 60 V were applied to titanium foil for 2 hr under 0.25 wt% NH_4F + 2 vol% $H_2O+C_2H_4(OH)_2$, TiO_2 with a nanotube structure was formed. The film, which had a large surface area, was used as an electron transport film in the DSSC. The DSSC device had a short-circuit current density (J_{sc}) of 12.52 mA cm^{-2}, a fill factor (FF) of 0.65, an open-voltage (V_{oc}) of 0.77 V, and a photocurrent efficiency of 6.3% under 100% AM 1.5 light. The internal impedance values under 100%, 64%, 11%, and 0% (dark) AM 1.5 light intensities were measured and simulated using the electrical impedance spectroscopy (EIS) technique. The impedance characteristics of the DSSC device were simulated using inductors, resistors, and capacitors. The Ti/TiO_2, TiO_2/Electrolyte, electrolyte, and electrolyte/(Pt/ITO) interfaces were simulated using an RC parallel circuit, and the bulk materials, such as the Ti, ITO and conducting wire, were simulated using a series of resistors and inductors. The impedance of the bulk materials was simulated using $L_0+R_0+R_b$, the impedance of the working electrode was simulated using $(C_1//R_1)//(R_a+(C_2//R_2)$, the electrolyte was simulated using $C_3//R_3$, and the counter electrode was simulated using $C_4//R_4$.

Keywords: DSSC; Anodic; TiO_2; Efficiency

Introduction

Following the report of a low-cost dye-sensitized solar cell (DSSC) in 1991 by O'Regan and Grätzel [1], the DSSC has been considered to be a promising candidate for next-generation solar cells [2]. The DSSC is gradually becoming popular and is being developed for its lower costs and simple manufacturing process [3,4]. A DSSC consists of an anode, an electrolytic solution and a cathode, wherein a semiconductor layer is formed on the surface of the anode and photosensitive dyes are absorbed. Traditionally, the electron-collecting layer (anode) of a DSSC is composed of randomly packed TiO_2 nanoparticles (NPs). When sunlight is irradiated through the transparent anode (front illumination), the best photovoltaic power conversion efficiency (η) of a NP-DSSC device has reached $\eta \sim 11\%$ [5–7]. Electrons transfer faster in TiO_2 nanotubes (NTs) than in TiO_2 NPs. To improve charge-collection efficiency by promoting faster electron transport and slower charge recombination, TiO_2 NTs have been produced using films constructed of oriented one-dimensional (1D) nanostructures. The amount of electron-hole (e^-/h^+) pairs that recombine is expected to be reduced in the one-dimensional channel for charge carrier transport. For example, Zhu [8] reported that recombination in the NT films is 10 times slower than in the NP films. Because of the performance drawbacks that result from substantial light scattering from the Pt-coated counter electrode and the light absorption of the iodine-based electrolyte, the back-illuminated DSSC has significantly lower efficiency than its front-illuminated counterpart. Although back-side illumination involves the aforementioned drawbacks, the NT-DSSCs that employ TiO_2 NT arrays on Ti foil as the working electrodes have many important intrinsic features

*Corresponding author. Tel.: +886 37 382383; fax: +886 37 382391.
**Corresponding author.
E-mail address: chentexas@gmail.com (C. Chon Chen).

0272-8842/$36.00
http://dx.doi.org/10.1016/j.ceramint.2012.04.079

that outperform conventional NP-DSSCs. For example, fabricating the anode for a NT-DSSC is considerably easier and more cost-effective than that of a NP-DSSC. In our previous paper, the photovoltaic power conversion efficiency (back illumination) of a NT-DSSC device has reached $\eta \sim 7\%$ [9].

In principle, electrochemical impedance spectroscopy (EIS) measurements cover a broad frequency range that may provide information about the electron transport interfaces and the charge transfer characteristics [10–12]. The DSSC has been analyzed using the transmission line model, which describes the electron transport and charge recombination in the nanoparticles and the films of nanotubes [13–16]. Kern [17] indicated that the characteristics of the Nyquist plot in the low-frequency range correspond to the electrolyte, whereas the middle-frequency range reflects the anode, and the high-frequency range corresponds to the cathode. Hoshikawa [18] also reported that the semicircles of ω_1, ω_2, ω_3, and ω_4 were attributable to the electron transfer at the transparent conduction oxide (TCO)/TiO_2 interface, the electron transfer in TiO_2 particles, the electron transfer at the TiO_2/I_3^- interface, and the diffusion impedance of I_3^- in the electrolyte, respectively.

This paper presents an analysis of the electrical impedance spectra, describes the ohmic resistance, electron transfer resistance, diffusion resistance, charge-transfer resistance, contact capacitance, chemical capacitance, electrolysis capacitance, double-layer capacitance, ohmic inductance, and inductive inductance in a NT TiO_2 DSSC under various simulated AM 1.5 light intensities.

Experimental

The ordered channel-array of anodic titanium oxide (ATO) was fabricated by anodizing titanium (Ti) foil (Aldrich, 99.7% purity). The Ti foil was first thoroughly electropolished [19] and etched with 5 vol.% HF for 5 min to enhance the ATO film growth on the Ti substrate. The growth of the TiO_2 NT was then achieved by anodization of the electrolyte (pH = 6.8), which consisted of 0.5 wt% ammonium fluoride (NH_4F, 99.9%) and 2 wt% H_2O in ethylene glycol ($C_2H_4(OH)_2$) as a solvent, through the application of 1 hr potentiostat (60 V) and 5 hr galvanostatic anodization (4.44 mA cm^{-2}). After the ATO films were formed from the anodization process, the samples were then annealed in air in a furnace for 450 °C for 3 hr to form the anatase phase ATO. The porous bundles of film were removed using ultrasonic vibration. The micromorphology and composition of the ATO were analyzed using a scanning electron microscope (SEM, JEOL 6500).

An indium-doped tin oxide (ITO) glass, which was coated with platinum (Pt) particles by sputtering, was used as a counter electrode. An electrolyte containing 0.5 M (lithium iodide) LiI and 0.05 M iodine (I_2) in acetonitrile (CH_3CN, 99.9%) was introduced into the electrodes. To fabricate the NT-DSSC device, the TiO_2 NT film was soaked in ethanol containing 5×10^{-4} M $RuL_2(NCS)_2$ (N3 dye) for 7 hr to absorb the N3 dye. We assembled the working and counter electrodes in a sandwich-type cell and sealed it with a hot-melt film (SX1170, Solaronix, thickness 25 μm). The photocurrent was produced using a HP model 4140B measuring unit. The amount of N3 dye absorbed by the TiO_2 NT was measured using UV-visible-NIR spectrophotometers (Jasco, V-570) at room temperature. The photocurrent conversion efficiency was tested under an AM 1.5 (300 W, 91160-Oriel Solar Simulator, 100 mw cm^{-2}) on a 0.28 cm^2 sample area [9,20].

The EIS measurements were performed using an Impedance Measuring Unit (IM 6) from Zahner. The electrochemical measurements were performed in two electrode configurations: the Pt/ITO electrode as a counter electrode and the dye/TiO_2 NT/ Ti as a working electrode. The impedance measurement of the cells was recorded over a frequency range of 5 MHz to 1 MHz with ac amplitude of 10 mV under various intensities of light from the AM 1.5 solar simulator. The EIS data were analyzed using the equivalent circuit model and fitted using the program Microsoft Excel.

Results and Discussion

TiO_2 NT Processing

The annealed titanium foil has the α phase crystal structure, on which the TiO_2 NT is grown on the surface of the flat grains. To control the quality of the surface roughness, the titanium surface was thoroughly electropolished (EP) and etched. Fig. 1(a) shows the optical microscopy (OM) morphology of the Ti foil surface after electro-polishing; a clean surface with grains (30 to 100 μm) and grain boundaries was observed. Furthermore, deep grain boundaries and pits were present on the EP surface after etching with 5 vol% HF for (b) 1 min, (c) 3 min, and (d) 5 min. A rougher Ti surface provides better adherence of the TiO_2 NT to Ti; for example, the surface of EP Ti should first be etched for 5 min, then a 70 μm thickness TiO_2 NT film has good adherence to the Ti surface. In the TiO_2 NT process, the other objective is to increase the growth rate of the NTs. In our process, we applied a constant voltage (60 V, 1 hr) and a constant current (4.44 mA cm^{-2}, 5 hr) during the anodization process and observed the formation of a 70 μm thick TiO_2 NT film after 6 hr. In the anodization, the ordered and patterned TiO_2 NTs on the Ti substrate are first obtained from the potentiostat, and when the power changed is changed to the galvanostat, the growth rate of the TiO_2 NTs is increased.

Fig. 2 compares the anodization time-current, time-voltage, and time-impedance curves in the galvanostatic and potentiostatic states; in the galvanostatic curve in Fig. 2(a), **(i)** the current increases (① to ②) with the anodization time when the applied voltage is increased from 0 to 60 V, **(ii)** the current decreases (② to ③) at a constant voltage of 60 V for 1 hr, **(iii)** the current increases (③ to ④) to a constant current, **(iv)** the current remains constant (④ to ⑤) for 5 hr, and **(v)** the current decreases to

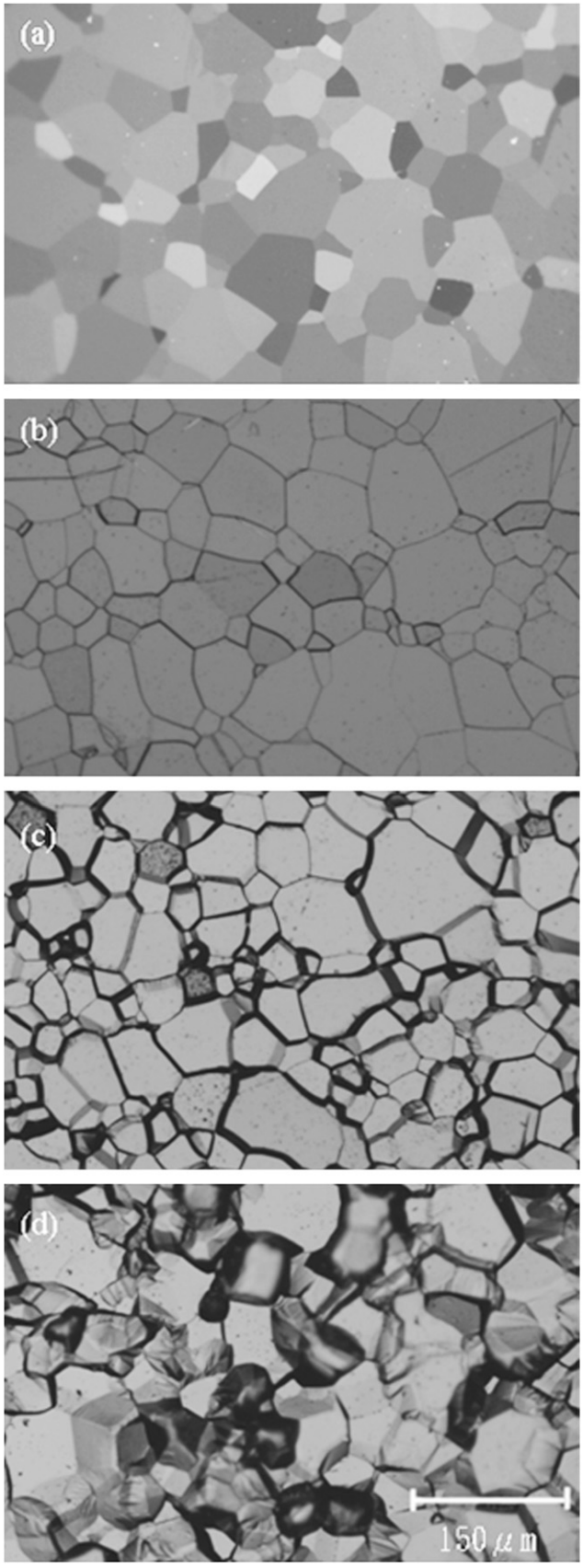

Fig. 1. OM images that reveal the surface morphology of the Ti foil (a) after electro-polishing, which has grain sizes between 30 and 120 μm; furthermore, deep grain boundaries and pits are present on the surface after etching with 5 vol.% HF for (b) 1 min, (c) 3 min, and (d) 5 min.

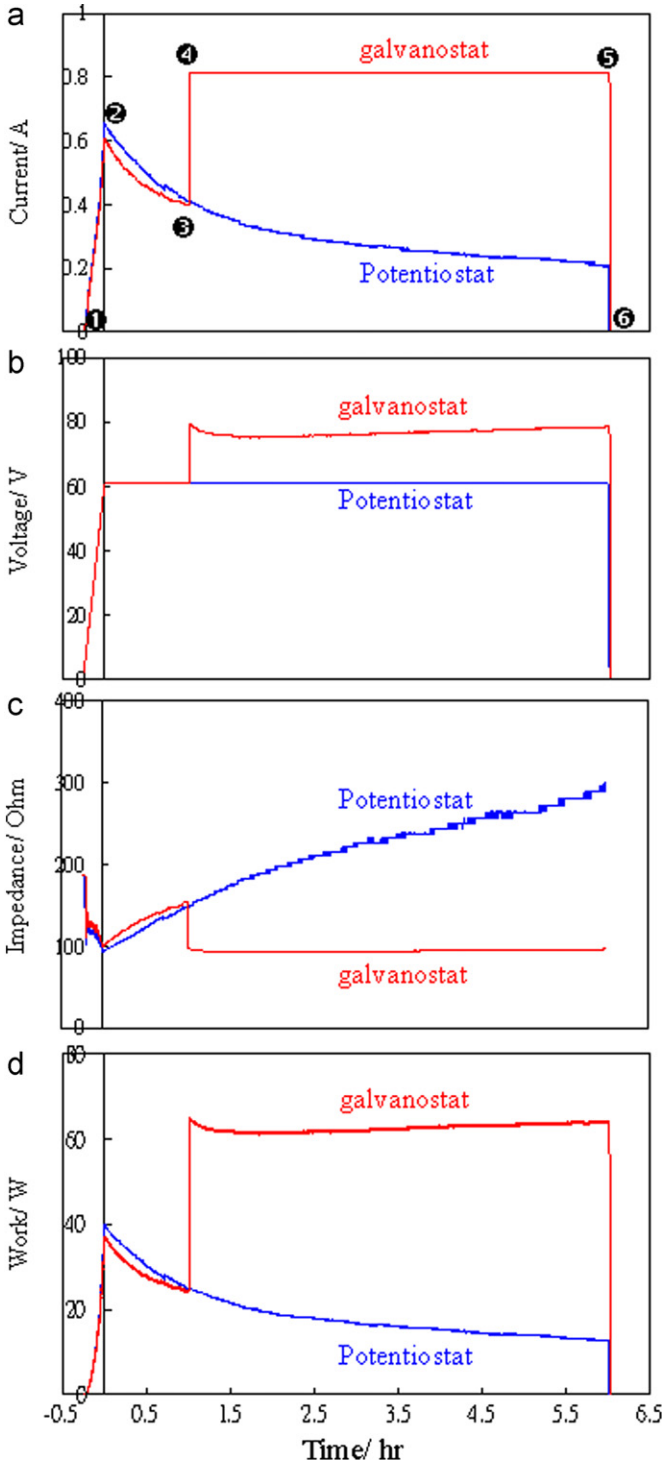

Fig. 2. The anodization time-current, time-voltage, and time-impedance curves in the galvanostat and potentiostatic states; (a) in the galvanostatic state, the current increases (① to ②) with increasing anodization time when the applied voltage increases from 0 to 60 V, current decreases (② to ③) at a constant voltage of 60 V for 1 hr, current increases (③ to ④) to a constant current, current remains at a constant value (④ to ⑤) for 5 hr, and current decreases to 0 (⑤ to ⑥) at the end. In the potentiostatic state, the current decreases with the increasing anodization time (from 1 to 6 hr). (b) The galvanostatic state was higher voltage applied than the potentiostatic state in the time-voltage curve; (c) the potentiostat operation mold has a higher impedance than the galvanostatic mold. (c) Galvanostat was higher work to ATO growth than potentiostat in the time-work curve.

0 (⑤ to ⑥) at the end. However, in the potentiostatic state, the current decreases with the increasing anodization time (from 1 to 6 hr). In Fig. 2(b), the galvanostatic state has a higher applied voltage than the potentiostatic state in the time-voltage curve; in Fig. 2(c), the potentiostatic state has a higher impedance value than the galvanostatic state; and in Fig. 2(d), the galvanostatic state reveals that higher work was input to the ATO growth than the potentiostatic state in the time-work curve. In the above results, the galvanostat has higher work and higher current but lower impedance compared to the potentiostat input in the anodization; therefore, the galvanostatic state has a higher growth rate than potentiostatic state. In our experience, when the anodization voltage and current density were controlled below 85 V and 6 mA cm^{-2}, the ordered TiO_2 NTs can be obtained.

TiO_2 NT Microstructure

Because both chemical and electrochemical etchings are performed on the anodic film, the top of the anodic film surface is always covered by an unwanted netted film. Although the top of the anodic film is in contact with the electrolyte, it is the metal itself under this film that is anodically oxidized. The top film is already an oxide. However, any oxide that is not integrated into the NT structure may deposit on the surface. To obtain a clean anodic film surface, we also treated the TiO_2 NT film with ultrasonic vibration for 2–3 min in deionized water. After the ultrasonic vibration treatment, a clean TiO_2 NT film is present on the Ti foil.

Fig. 3 presents SEM images that show a side view of the TiO_2 NT microstructures. (a) The length of the TiO_2 NT was 67.5 μm long after 1 hr potentiostatic and 5 hr galvanostatic anodization, and (b) shows porous and bundled films on the TiO_2 NT. (c) The length of the TiO_2 NT was 55.1 μm after the porous and bundled films were removed using ultrasonic vibration, and (d) shows small contact points between the TiO_2 NTs. To produce a good quality TiO_2 NT film, the substrate was pre-treated using etching processes, which enabled the TiO_2 NT to adhere well to the Ti surface, and the galvanostat operation mold can reduce the anodization time and the porous and bundled films on the TiO_2 NT. Fig. 4 presents a detailed SEM image of the TiO_2 NT microstructures; (a) TiO_2 NT with a 125 ± 5 nm pore diameter, 150 ± 5 nm pore distance and 20 ± 5 nm pore wall thickness, and a 5×10^9 cm^{-2} pore in the top view image; (b) a tubular structure in the side view image; (c) a pore and a tubular structure in the side view image; (d) a close view of the bottom of the tube in the side view image; (e) a barrier layer on the tube bottom; and (f) a pore and a barrier layer structure on the tube bottom. Fig. 5 presents SEM images of the TiO_2 NT, which has a larger pore on the top of the tube and a smaller pore on the bottom of the tube; (a) a 125 nm diameter pore on the top of the tube, (b) (c) 110 and 95 nm diameter pores near the top of the tube, (d) a 75 nm diameter pore near the bottom of the tube, and (e) a 50 nm diameter pore on the bottom of the tube. According to Figs. 4 and 5 (a)–(e), the TiO_2 NT has an open pore on the top of the tube, a close barrier layer on the bottom, a column structure on the outer tube, and a cone structure on the inner tube; a schematic diagram of the TiO_2 NT is shown in Fig. 5 (f).

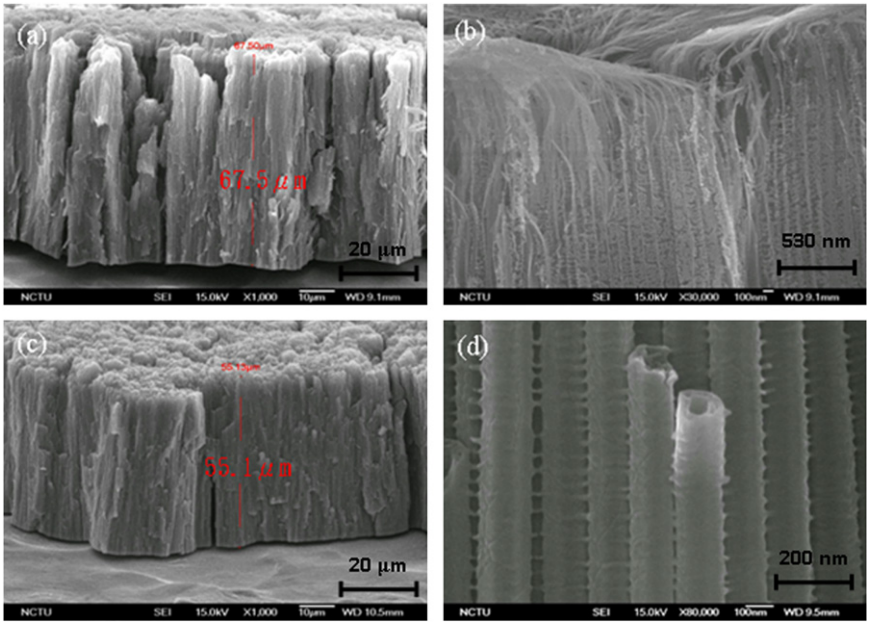

Fig. 3. SEM images that present the side view of the TiO_2 NT microstructure. (a) TiO_2 NT has a length of 67.5 μm after 1 hr potentiostatic and 5 hr galvanostatic anodization, (b) porous and bundled structures on the top, (c) a length of 55.1 μm after the porous and bundled films are removed using ultrasonic vibration, and (d) small contact points between the TiO_2 NTs.

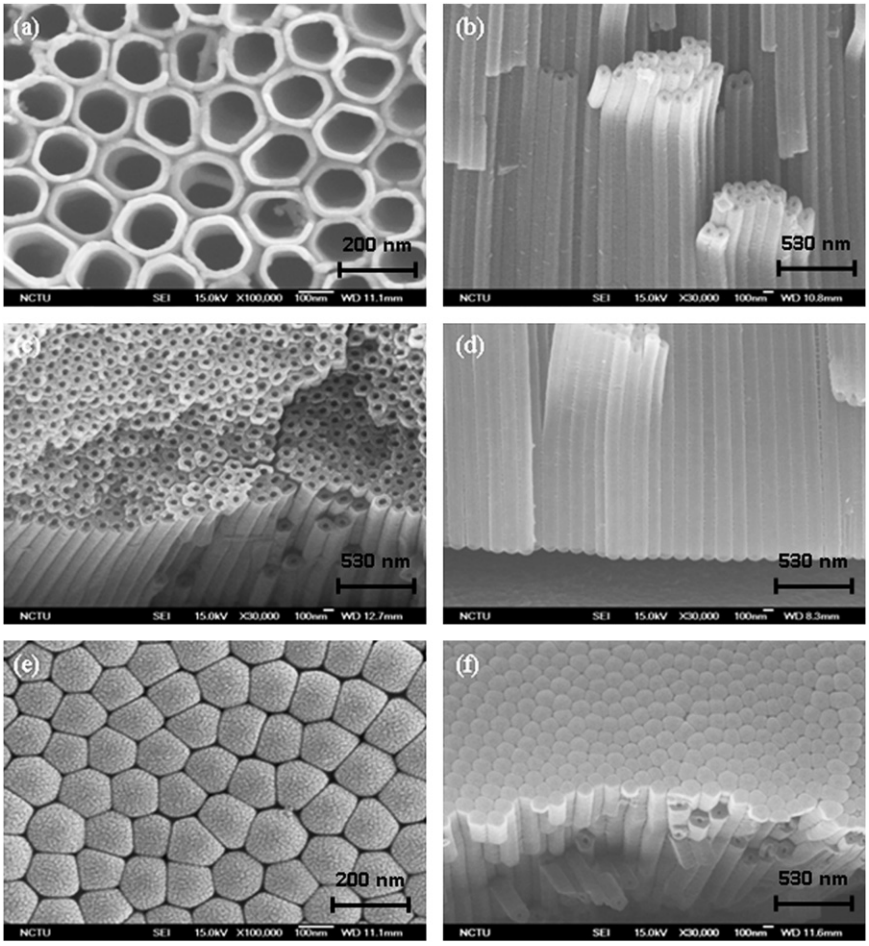

Fig. 4. SEM images that show the TiO_2 NT microstructures. (a) TiO_2 NTs with a 125 nm pore diameter in the top view image, (b) a tubular structure in the side view image, (c) a pore and a tubular structure in the side view image, (d) a close view of the bottom of the tube in the side view image, (e) a barrier layer on the bottom of the tube, and (f) a pore and a barrier layer structure on the bottom of the tube.

Performance of the TiO_2 NT DSSC under Various Intensities of Light

Fig. 6 shows the J-V curve of TiO_2 NT DSSC under various intensities of light from the AM 1.5; higher current densities and conversion efficiencies were observed with higher intensities of light on the DSSC. Table 1 presents the detailed analytical parameters of the J-V curves that were obtained under various intensities of light from the AM 1.5. The short current densities (J_{sc}), open voltages (V_{oc}), and the maximum working power (W_{mp}) increase as the light intensities increase, but the maximum impedance (R_{mp}) decreases. The internal impedance on the DSSC interfaces can also be detected, and they were analyzed in detail using the EIS technique. Fig. 7 presents Bode plots of the DSSC under various light intensities. There are three regions, 10^0–10^{-3} Hz, 10^0–10^4 Hz, and 10^4–10^6 Hz, that can be discriminated from the Bode plots. These regions reflect the impedances to the electrolyte, anode and cathode in the DSSC. The results from the Bode plot correspond to the maximum impedance in the J-V curve, which indicates that the impedances are reduced as the intensity of the sun light increases.

Fig. 8(a) presents a schematic diagram of the impedance structure of the DSSC. The internal impedances are comprised of at least twelve electrical components. The internal resistances of the electrodes or load wire were simulated using a resistor and the electron and charge transportation or diffusion between the interfaces was simulated using a RC parallel circuit. It was observed that the resistances of the titanium foil (R_0), transport wire and counter material (R_b), and a series of inductances (L_0) appeared as an ohmic impedance. The ohmic impedance value was independent of the intensity of the light. The other resistances, including the TiO_2 resistance (R_a), contact resistance (R_1), diffusion resistance (R_3), and charge-transfer resistance (R_2 and R_4) as the internal resistances, were affected by the intensity of the light, which is critical to the performance of the DSSC. The interface capacitances, including the contact capacitance (C_1), chemical capacitance (C_2), diffusion capacitance (C_3), and double-layer capacitance (C_4), are crucial for the charge transport performance on the interfaces of the DSSC. The ohmic inductance (L_0), which is expressed as the inductance in the loading wire, was present in the higher frequency region.

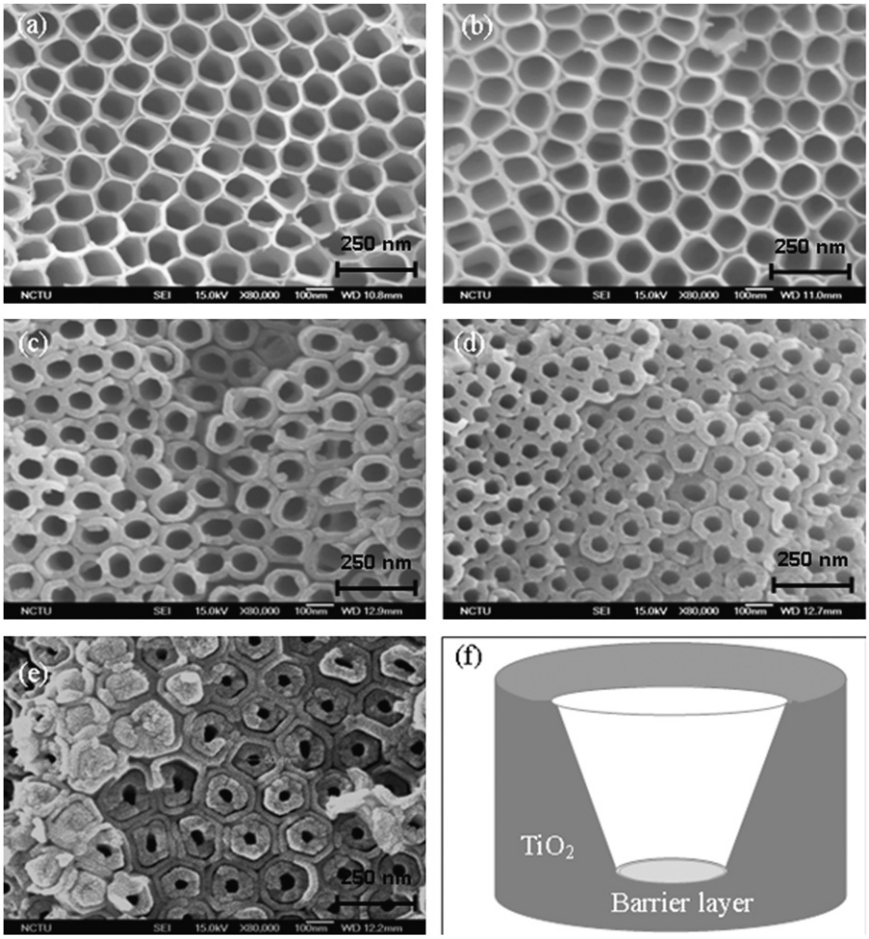

Fig. 5. SEM images that demonstrate that the TiO_2 NT has a larger pore on the top of the tube and a smaller pore on the bottom of the tube; (a) a 125 nm diameter pore on the top of the tube, (b) (c) 110 and 95 nm diameter pores near the top of the tube, (d) a 75 nm diameter pore near the bottom of the tube, (e) a 50 nm diameter pore on the bottom of the tube, and (f) a schematic diagram that shows that the TiO_2 NT has an open pore on the top, a close barrier layer on the bottom, a column structure on the outer tube, and a cone structure on the inner tube.

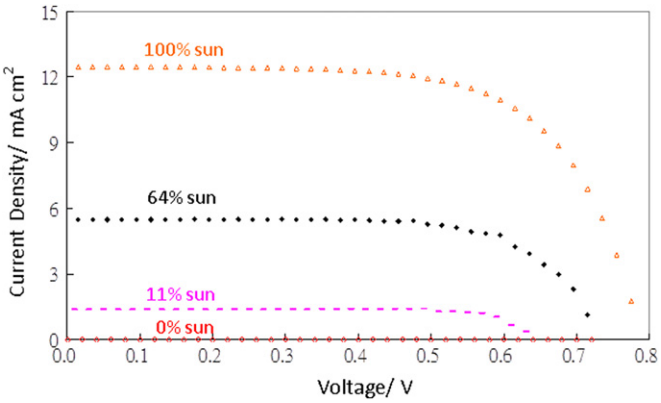

Fig. 6. J-V curves of the TiO_2 NT DSSC under various intensities of light using the AM 1.5; the highest current density was observed when the highest intensity of light from the AM 1.5 was illuminated on the DSSC.

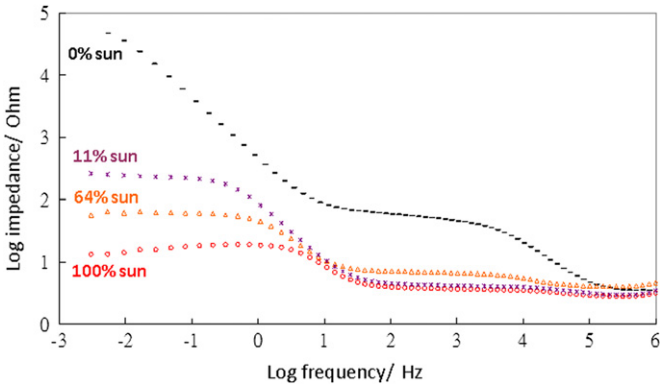

Fig. 7. Bode plots of the TiO_2 NT DSSC under various intensities of light using the AM 1.5; the highest impedance value was observed when the lowest intensity of light from the AM 1.5 was illuminated on the DSSC.

The R_a reflects the internal resistance of the TiO_2 film, and a lower R_a value favors electron transport from the dye to the Ti foil. The $R_1//C_1$ ratio reflects the interface characteristics of Ti/TiO_2, and when a poor contact is established between the Ti and TiO_2 interface, a higher impedance was displayed. This result indicated that the electron has a difficult transport path from the Ti to the TiO_2 film (a large R_1 can be observed) and a large quantity of charges stay on the Ti/TiO_2 interface (a large C_1 can be observed). The $R_2//C_2$ ratio reflects the interface

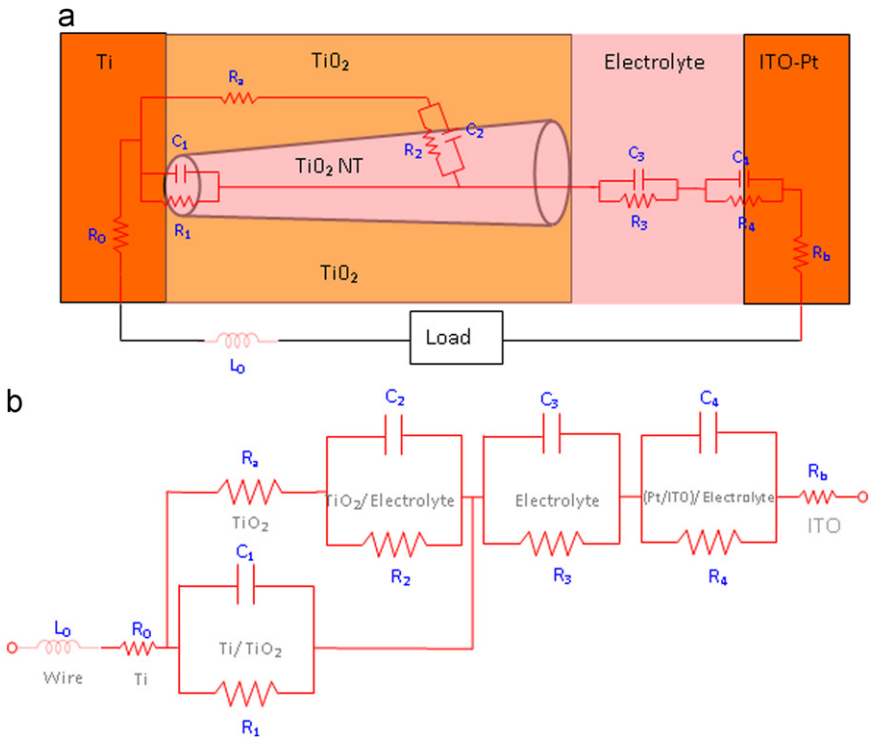

Fig. 8. Schematic diagram of (a) DSSC structure that can be simulated using a resistor, capacitor, and an inductor. Each individual interface, including the Pt/ITO - electrolyte, electrolyte - TiO_2, and TiO_2 – Ti, can be simulated using a RC parallel circuit; the bulk materials of Pt/ ITO, Ti, and conducting wire can be simulated using a series of resistors and inductors; (b) equivalent circuit used for modeling the EIS of the DSSC. The impedance of the bulk is simulated using a series of $L_0+R_0+R_b$, the impedance of the anode is simulated by $(C_1//R_1)//(R_a+(C_2//R_2)$, the electrolyte is simulated by $C_3//R_3$, and the cathode is simulated by $C_4//R_4$.

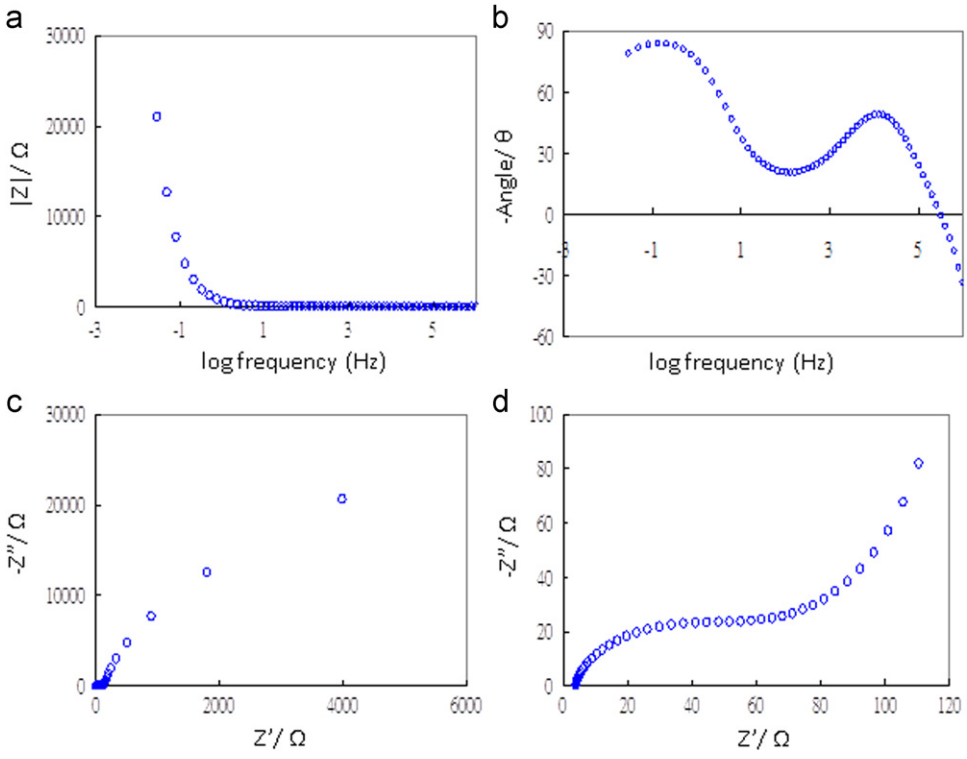

Fig. 9. EIS spectra of the DSSC without illumination; (a) Bode plot, (b) phase angle plot, (c) Nyquist plot, (d) Nyquist plot in a higher range of frequencies.

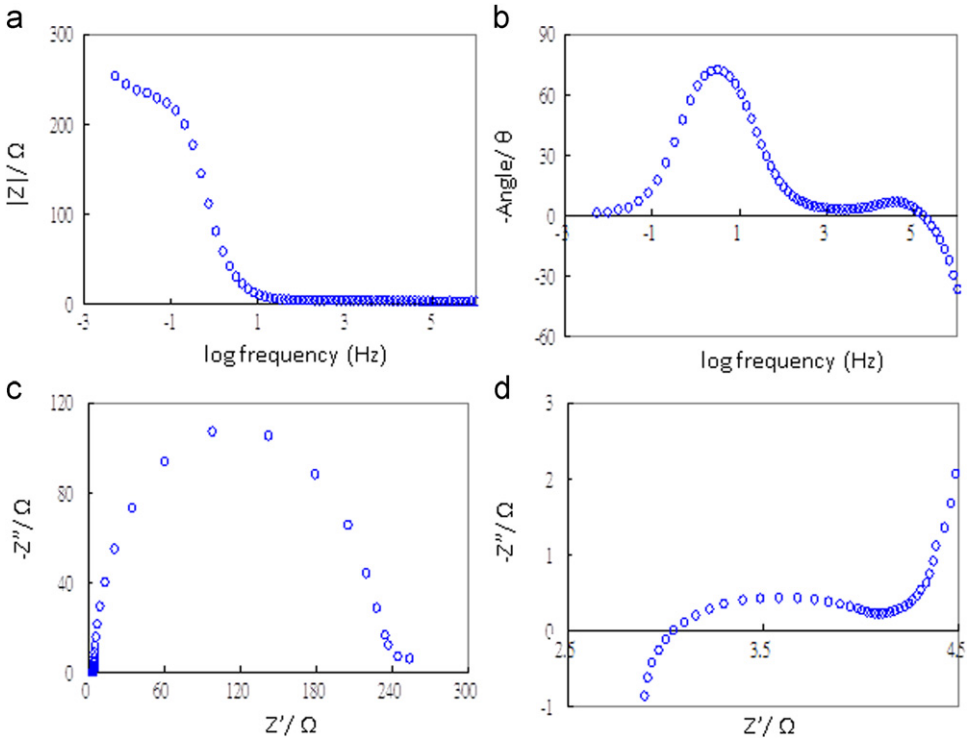

Fig. 10. EIS spectra of the DSSC under 11% of illumination using the AM 1.5; (a) Bode plot, (b) phase angle plot, (c) Nyquist plot, (d) Nyquist plot in a higher range of frequencies.

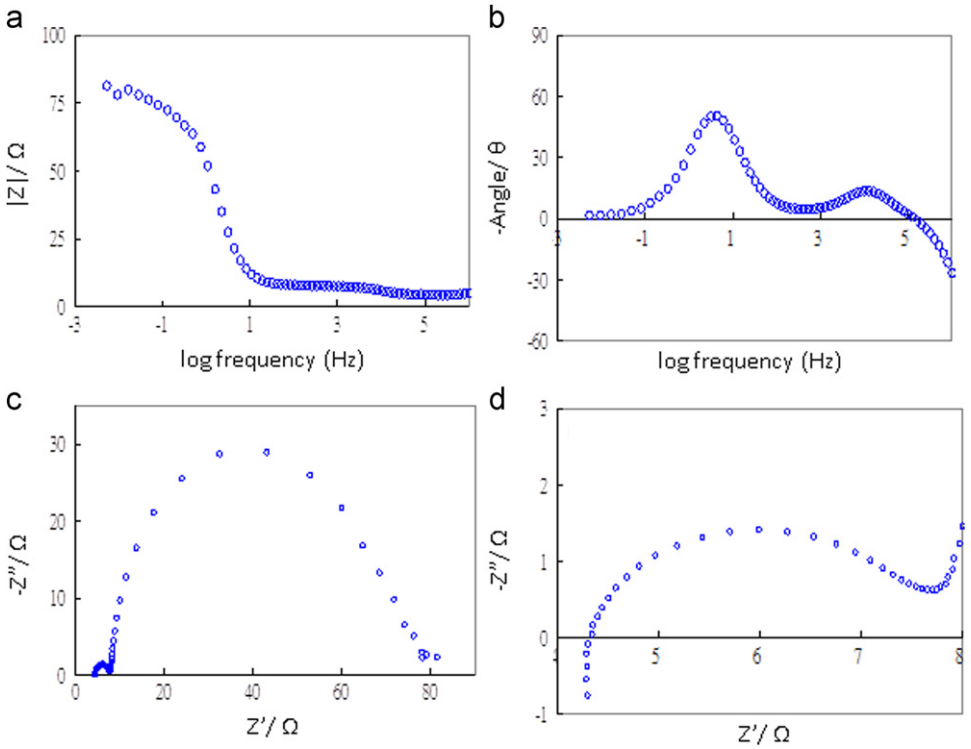

Fig. 11. EIS spectra of the DSSC under 64% of illumination using the AM 1.5; (a) Bode plot, (b) phase angle plot, (c) Nyquist plot, (d) Nyquist plot in a higher range of frequencies.

characteristics of the TiO_2/electrolyte. When a lower electron transport rate from TiO_2 to electrolyte was displayed, higher R_2 and C_2 values were observed. The $R_3//C_3$ ratio reflects the ion transportation characteristics in the electrolyte. When faster ion transportation rates for I^- and I_3^- in the electrolyte were displayed, lower R_2 and C_2 values were observed.

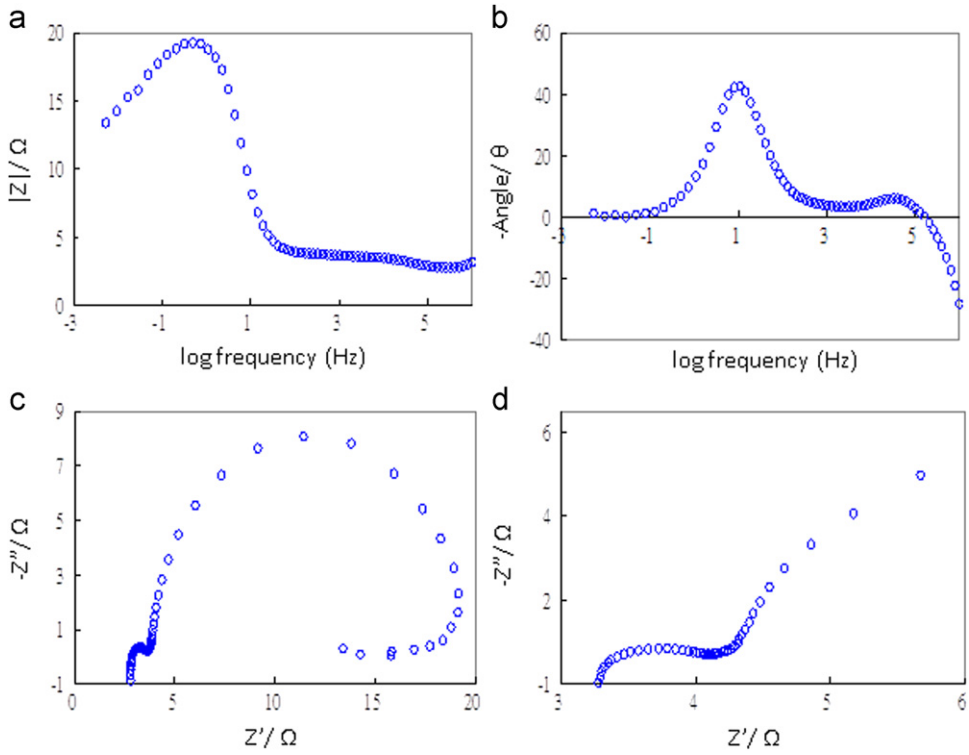

Fig. 12. EIS spectra of the DSSC under 100% of illumination using the AM 1.5; (a) Bode plot, (b) phase angle plot, (c) Nyquist plot, (d) Nyquist plot in a higher range of frequencies.

The $R_4//C_4$ ratio reflects the interface characteristics of the counter electrode and the electrolyte. When a higher reduction rate from the electrolyte to the counter electrode was displayed, lower R_4 and C_4 values were observed.

The DSSC equivalent circuit is illustrated in Fig. 8(b), and the equivalent impedance can be expressed as $(L_0+R_0+R_b)+\{[(C_1//R_1)//(R_a+(C_2//R_2))\}+(C_3//R_3)+(C_4//R_4)$. In the equivalent circuit, the $L_0+R_0+R_b$ impedance was detected in the higher range of frequencies and the $L_0+R_0+(R_1//R_a)+R_2+R_3+R_4+R_b$ impedance was detected on the real axis in lower range of frequencies. However, the capacitance values of C_1, C_2, C_3, C_4 were detected on the real and imaginary axes in the middle range of frequencies. Because the counter electrode in $R_3//C_3$ has the lowest impedance, the electrolyte in $R_3//C_3$ has the highest Warburg diffusion impedance, and the anode in $(C_1//R_1)//(R_a+(C_2//R_2)$ has a middle impedance; the ordering of semicircles of the counter electrode, anode, and electrolyte appear in the Nyquist plot from the highest to lowest frequencies.

Fig. 9 presents the EIS spectra of the DSSC without illumination (under dark conditions); (a) the Bode plot has a higher impedance in lower range of frequencies, which indicates that the DSSC has a large impedance in lower range of frequencies; (b) the phase angle plot has a higher angle value in lower range of frequencies, which indicates that the DSSC has a large capacitance value in lower range of frequencies; (c) Nyquist plot in the higher range of frequencies; and (d) Nyquist plot in lower range of frequencies. Figs. 10–12 also present the EIS spectra of the DSSC under 11%, 64%, and 100% of light illumination using the AM 1.5. According to the Bode and Nyquist plots, the internal-impedance of the DSSC was decreased (electron transport rate increased) after light illumination. Furthermore, based on the phase angle plot, the phase angle was decreased (charge transfer rate increased) after light illumination.

Impedance Evaluation by EIS Modeling and Fitting

Because there are considerably different impedance values between the DSSC interfaces and a larger impedance semicircle always covers a smaller semicircle, it is difficult to observe each independent semicircle from the raw data in the Nyquist plot. To separate each individual semicircle of the interface impedance, the experimental raw data should be simulated and fitted using the equivalent circuit model. The DSSC equivalent circuit model can be constructed using a series of loading wire $(L_0+R_0+R_b)$, working electrode $\{[(C_1//R_1)//(R_a+(C_2//R_2))\}$, electrolyte $(C_3//R_3)$, and counter electrode $(C_4//R_4)$. Based on the impedance properties of $Z_R=R$, $Z_C=(j\omega C)^{-1}$, and $Z_L=j\omega L$, the real and imaginary components of equivalent circuit can be separated and illustrated, as in Table 2. Therefore, the individual interface impedance can be analyzed in detail using the experimental data and fitting results.

Figs. 13–16 present the experimental (O) and fitting (——) data of the DSSC impedance spectra under dark (0%), 11%, 64%, and 100% AM1.5 lighting;

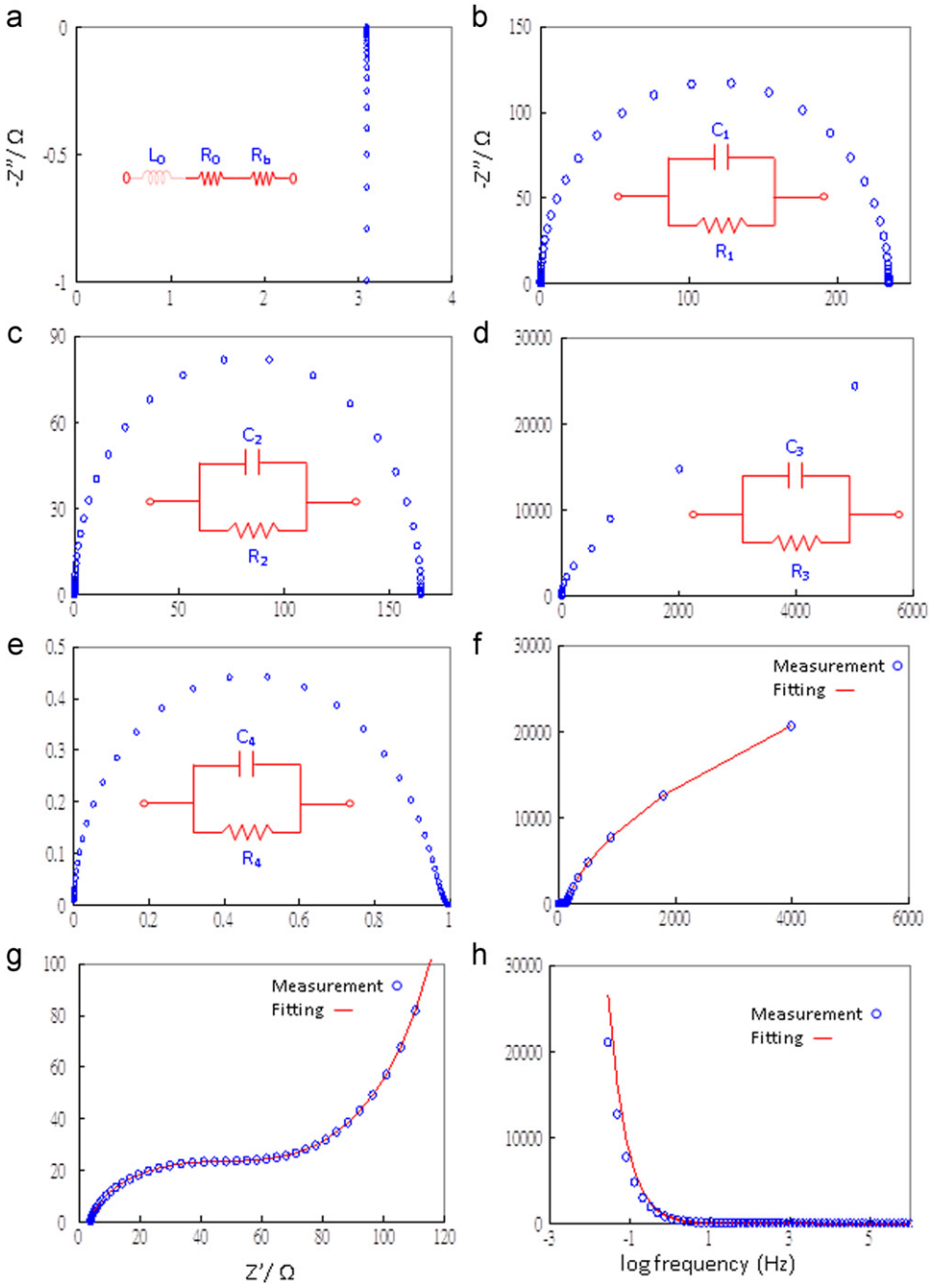

Fig. 13. Simulated EIS spectra and the fitted spectra of the DSSC without illumination, (a) simulated spectra of the loading wire, (b) simulated spectra of the Ti/TiO_2, (c) simulated spectra of the Ti/Electrolyte, (d) simulated spectra of the electrolyte, (e) simulated spectra of the Electrolyte/(Pt/ITO), (f) Nyquist plot fitting, (g) Nyquist plot in a higher range of frequencies fitting, (h) phase angle plot fitting.

(a) loading wire impedance simulation, (b) Ti/TiO_2 interface impedance simulation, (c) Ti/Electrolyte interface impedance simulation, (d) electrolyte impedance simulation, (e) electrolyte/(Pt/ITO) interface impedance simulation, (f) Nyquist plot fitting, (g) Nyquist plot in the higher range of frequencies, and (h) phase angle plot fitting. The simulation elements include L_0 (μH), R_0 (Ω), R_a (Ω), R_b (Ω), R_1 (Ω), R_2 (Ω), R_3 (Ω), R_4 (Ω), C_1 (μF), C_2 (μF), C_3 (μF), and C_4 (μF). The fitting results from the EIS data and equivalent circuit model are presented in Table 3. The results indicated that (1) the ohmic inductance (L_0; 0.4–0.5 μH), ohmic resistance (R_0, 0.23–0.28 Ω), and counter resistance (R_b, 2.5–3.1 Ω) are independent of the intensity of the light; (2) the TiO_2 film has a photo-excitation semiconductor property whose resistance value was decreased after illumination (R_a from 10 to 2.8 Ω); (3) Ti/TiO_2 interface electron and charge transfer rate increased with an increase in the intensity of the light (R_1 from 5 to 0.04 Ω, C_1 from 3 to 0.001 μF); (4) TiO_2 electrolyte interface electron and charge transfer rates

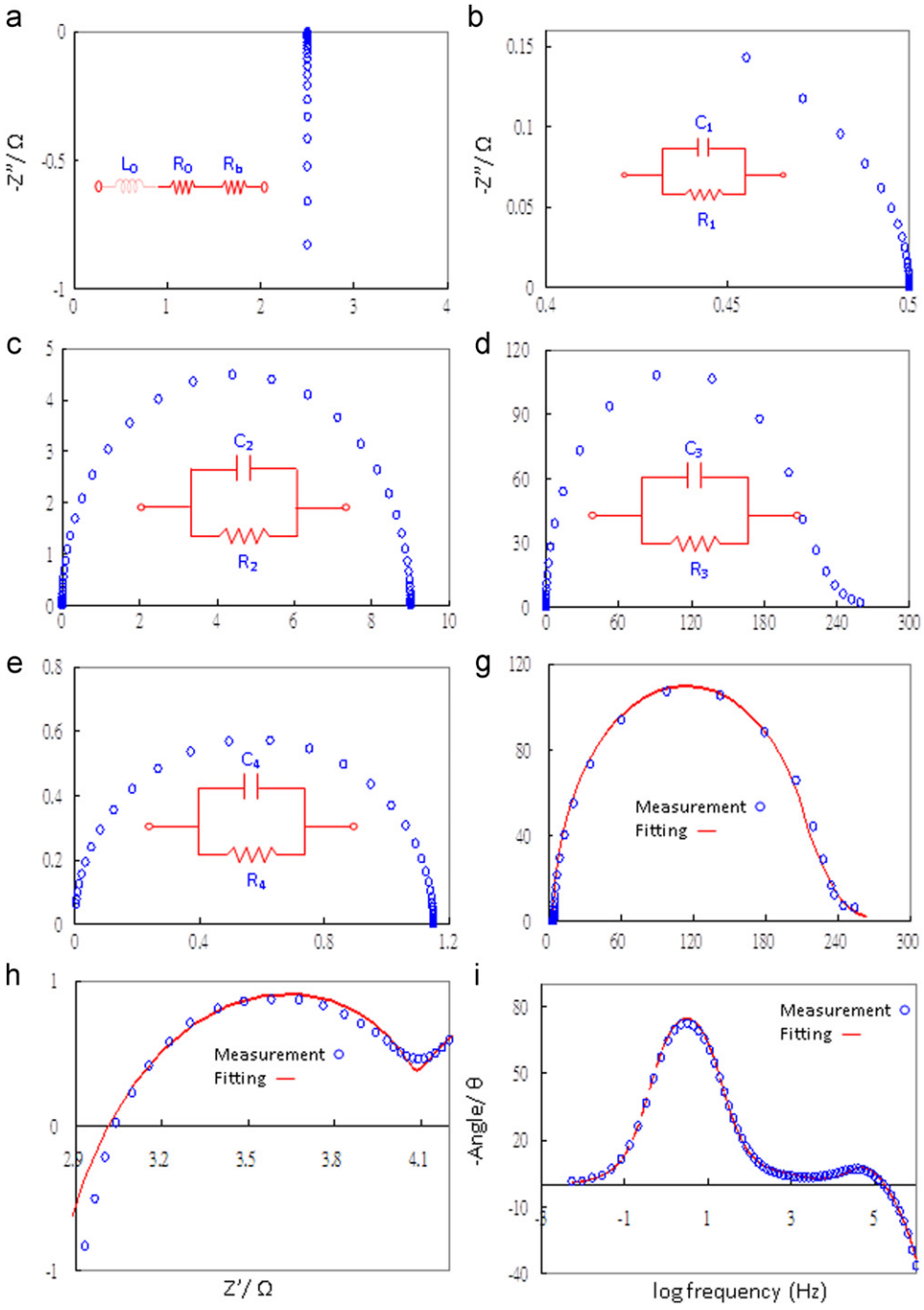

Fig. 14. Simulated EIS spectra and the fitted spectra of the DSSC under 11% of illumination using the AM 1.5, (a) simulated spectra of the loading wire, (b) simulated spectra of the Ti/TiO_2 interface, (c) simulated spectra of the Ti/Electrolyte interface, (d) simulated spectra of the electrolyte, (e) simulated spectra of the electrolyte/(Pt/ITO) interface, (f) Nyquist plot fitting, (g) Nyquist plot in a higher range of frequencies fitting, (h) phase angle plot fitting.

increased with an increase in the intensity of the light (R_2 from 50 to 4Ω, C_1 from 6000 to 0.08F); (5) an oxidation reaction of $3I^- DoubleLongRightArrow;^{Oxidation} I_3^- + 2e^-$ occurs close to the working electrode side, and a reduction reaction of $I_3^- + 2e^- DoubleLongRightArrow;^{Reduction} 3I^-$ occurs close to the counter electrode side; therefore, I_3^- and I^- ions absorb on the surfaces of the working and counter electrodes, respectively. Moreover, the electrolyte capacitance (C_3) was increased from 200 to 1750 μF, and the electrolyte resistance (R_3) was decreased from 66000 to 16 Ω during illumination. (6) The Electrolyte/counter interface has a large quantity of I_3^- during illumination, which increased C_4 increased from 2 to 5.5 μF with an increase in the intensity of the light. Furthermore, the waiting electron, which move and combine with I_3^- on the surface of the counter electrode, decreased R_4 from 32 to 0.35 Ω.

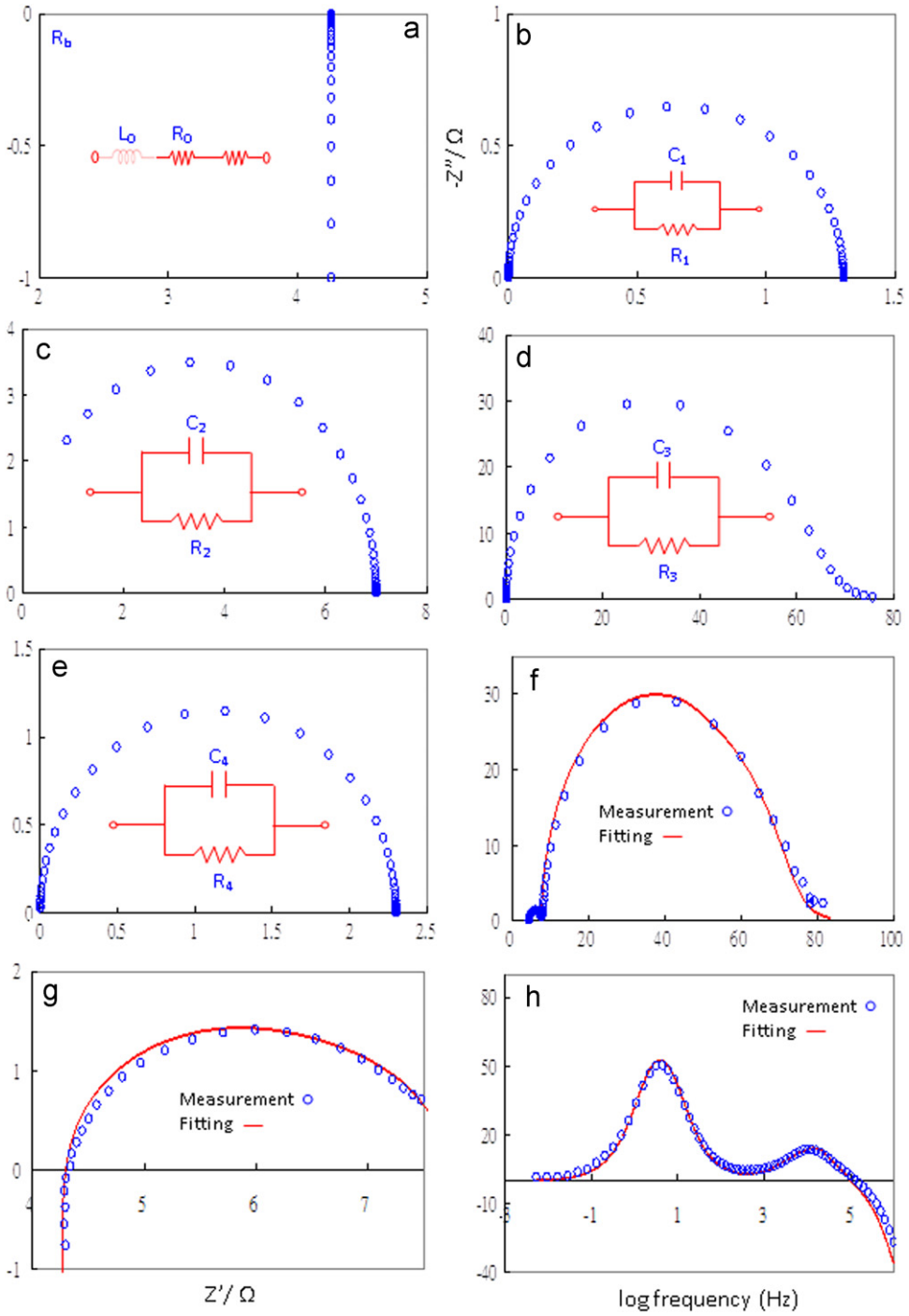

Fig. 15. Simulated EIS spectra and the fitted spectra of the DSSC under 64% of illumination using the AM 1.5, (a) simulated spectra of the loading wire, (b) simulated spectra of the Ti/TiO_2 interface, (c) simulated spectra of the Ti/electrolyte interface, (d) simulated spectra of the electrolyte, (e) simulated spectra of the electrolyte/(Pt/ITO) interface, (f) Nyquist plot fitting, (g) Nyquist plot in a higher range of frequencies fitting, and (h) phase angle plot fitting.

Conclusions

During anodization, the TiO_2 NT has a conical column structure that consists of an inner tube, a straight outer tube, a compact barrier layer on the bottom, an ordering of outer pores with a pore diameter of 120 ± 5 nm, a 150 ± 5 nm pore distance, a 20 ± 5 nm pore wall thickness, and a pore area of 8×10^9 cm^{-2}. Based on the calculations, a 100 μm TiO_2 NTs film with a 1 cm^2 sample area has a surface area of 5966 cm^2, which offers a large surface for the electron transport film of the DSSC. The internal impedances and the electrochemical characteristics of the charge transfer at the DSSC interface are important conditions for the efficiency of the DSSC. In this paper,

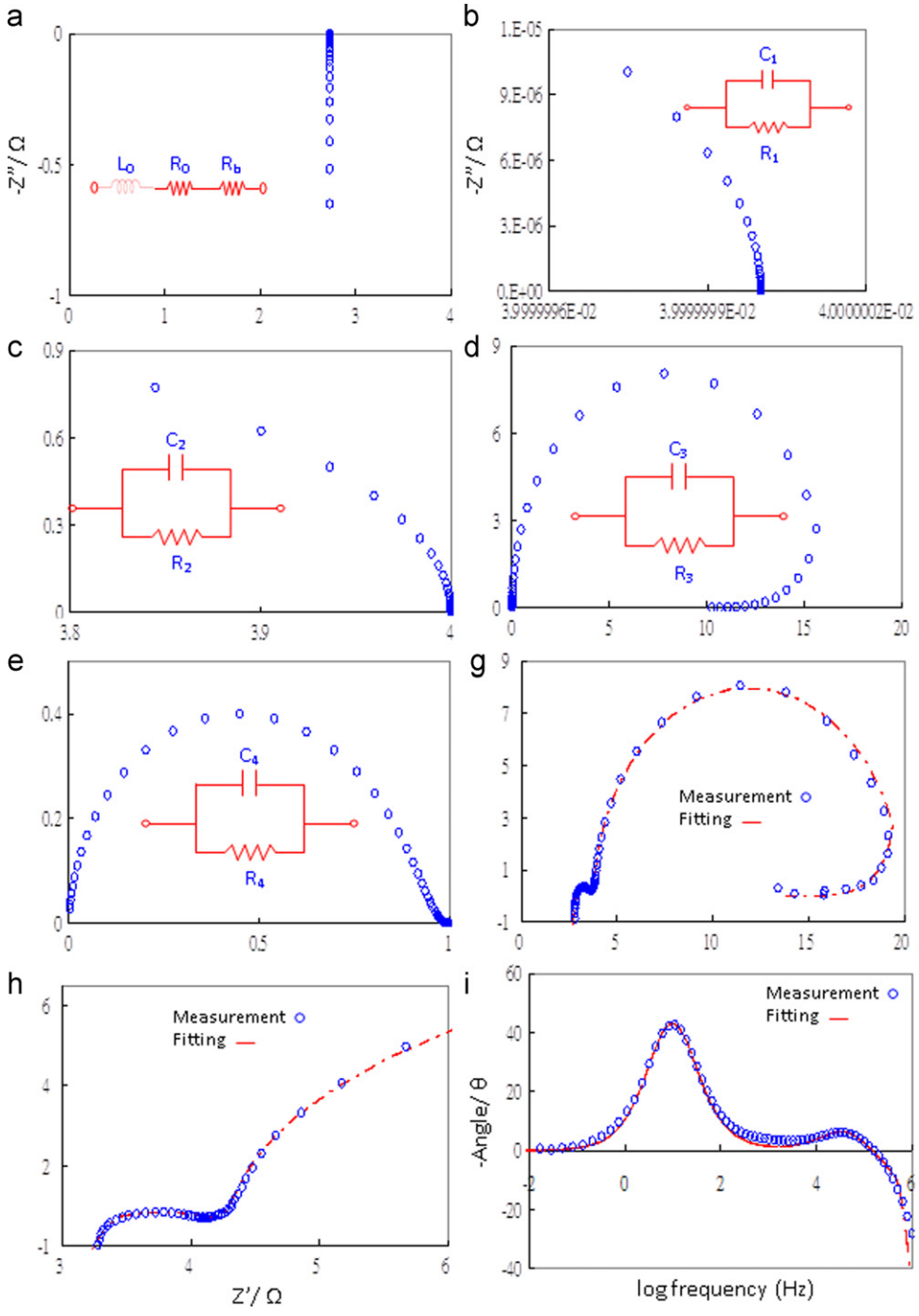

Fig. 16. Simulated EIS spectra and the fitted spectra of the DSSC under 100% of illumination using the AM 1.5, (a) simulated spectra of the loading wire, (b) simulated spectra of the Ti/TiO_2 interface, (c) simulated spectra of the Ti/electrolyte interface, (d) simulated spectra of the electrolyte, (e) simulated spectra of the electrolyte/(Pt/ITO) interface, (f) Nyquist plot fitting, (g) Nyquist plot in a higher range of frequencies fitting, and (h) phase angle plot fitting.

the internal resistance of the electrodes and the interface impedances were analyzed using AC Impedance measurements, which provides results that are helpful for improving the DSSC conversion efficiency. Based on the results from the AC impedance measurements, DSSC must satisfy the following conditions to achieve a higher conversion efficiency: (1) shorten the length of the contact wires (reducing L_0), (2) reduce the resistance of the electrodes, (3) establish a good contact point between the electrodes (reducing R_0 and R_b), (4) increase the crystallinity and ordering microstructure of the electron transfer film (reducing R_a), (5) increase the contact between the anode and electron transfer film (reducing R_1 and C_1), (6) match the energy levels between the sensitized dye and electron transfer film (increasing R_2 and C_2), (7) increase the ion diffusion rate in the electrolyte (reducing R_3 and R_4), (8)

increase the catalytic rate on the surface of the counter electrode (reducing C_4), and (9) reduce the electron transfer from the electron transfer film to the electrolyte ($R_2 > R_1$ and R_a).

Acknowledgements

The authors gratefully appreciate the financial support of the National Science Council of ROC under the contract No. 100-2627-M-239-001.

References

[1] B. O'Regan, M. Grätzel, A low-cost, high-efficiency solar cell based on dye sensitized colloidal TiO_2 films, Nature 353 (1991) 737–740.
[2] M. Grätzel, Photoelectrochemical Cells, Nature 414 (2001) 338–344.
[3] H.G. Bang, J.K. Chung, R.Y. Jung, S.Y. Park, Effect of acetic acid in TiO_2 paste on the performance of dye-sensitized solar cells, Ceram. Int. 38S (2012) S511–S515.
[4] M.N. An'amt, S. Radiman, N.M. Huang, M.A. Yarmo, N.P. Ariyanto, H.N. Lim, M.R. Muhamad, Sol–gel hydrothermal synthesis of bismuth–TiO_2 nanocubes for dye-sensitized solar cell, Ceram. Int. 36 (2010) 2215–2220.
[5] M.K. Nazeeruddin, F.D. Angelis, S. Fantacci, A. Selloni, G. Viscardi, P. Liska, S. Ito, B. Takeru, M. Grätzel, Combined experimental and DFT-TDDFT computational study of photoelectrochemical cell ruthenium sensitizers, J. Am. Chem. Soc. 127 (2005) 16835–16847.
[6] M. Wei, Y. Konishi, H. Zhou, M. Yanagida, H. Sugihara, H. Arakawa, Highly efficient dye-sensitized solar cells composed of mesoporous titanium dioxide, J. Mater. Chem. 16 (2006) 1287–1293.
[7] N. Koide, A. Islam, Y. Chiba, L. Han, Improvement of efficiency of dye-sensitized solar cells based on analysis of equivalent circuit, J, Photochem. Photobio. A 182 (2006) 296–305.
[8] K. Zhu, N.R. Neale, A. Miedaner, A.J. Frank, Enhanced charge-collection efficiencies and light scattering in dye-sensitized solar cells using oriented TiO_2 nanotubes arrays, Nano Lett 7 (2007) 69–74.
[9] C.C. Chen, H.W. Chung, C.H. Chen, H.P. Lu, C.M. Lan, S.F. Chen, L. Luo, C.S. Hung, W.G. Diau, Fabrication and Characterization of Anodic Titanium Oxide Nanotube Arrays of Controlled Length for Highly Efficient Dye-Sensitized Solar Cells, J. Phys. Chem. C 112 (2008) 19151–19157.
[10] G. Kron, T. Egerter, J.H. Werner, U. Rau, Electronic Transport in dye-sensitized nanoporous tiO2 solar cells comparison of electrolyte and solid-state devices, J. Phys. Chem. B 107 (2003) 3556–3564.
[11] K. Schwarzburg, F. Willig, Diffusion impedance and space charge capacitance in the nanoporous dye-sensitized electrochemical solar cell, J. Phys. Chem. B 107 (2003) 3552–3555.
[12] C. He, L. Zhao, Z. Zheng, F. Lu, Determination of electron diffusion coefficient and lifetime in dye-sensitized solar cells by electrochemical impedance spectroscopy at high fermi level conditions, J. Phys. Chem. C 112 (2008) 18730–18733.
[13] L. Andrade, S.M. Zakeeruddin, M.K. Nazeeruddin, H.A. Ribeiro, A. Mendes, M. Grätzel, Influence of sodium cations of N3 dye on the photovoltaic performance and stability of dye-sensitized solar cells, Chem. Phys. Chem 10 (2009) 1117–1124.
[14] J. Bisquert, M. Grätzel, Q. Wang, F.F. Santiago, Three-channel transmission line impedance model for mesoscopic oxide electrodes functionalized with a conductive coating, J. Phys. Chem. B 110 (2006) 11284–11290.
[15] G. Franco, J. Gehring, L.M. Peter, E.A. Ponomarev, I. Uhlendorf, frequency-Resolved Optical Detection of Photo injected Electrons in Dye-Sensitized Nan crystalline Photovoltaic Cells, J. Phys. Chem. B 103 (1999) 692–698.
[16] F.F. Santiago, E.M. Berea, J. Bisquert, G.K. Moor, K. Shankar, C.A. Grimes, High carrier density and capacitance in TiO_2 nanotube arrays induced by electrochemical doping, J. Am. Chem. Soc. 130 (2008) 11312–11316.
[17] R. Kern, R. Sastrawan, J. Ferber, R. Stangl, J. Luther, Modeling and interpretation of electrical impedance spectra of dye solar cells operated under open-circuit conditions, Electrochimica Acta 47 (2002) 4213–4225.
[18] T. Hoshikawa, M. Yamada, R. Kikuchi, K. Eguchi, Impedance Analysis of Internal Resistance Affecting the Photoelectrochemical Performance of Dye-Sensitized Solar Cells, J. Electrochem. Soc. 152 (2005) E68–E73.
[19] C.C. Chen, J.H. Chen, C.G. Chao, W.C. Say, Electrochemical Characteristics of Surface of Titanium Formed by Electrolytic Polishing and Anodizing, J. Mater. Sci. 40 (2005) 4053–4059.
[20] C.C. Chen, W.D. Jehng, L.L. Li, W.G. Diau, Enhanced Efficiency of Dye-sensitized Solar Cells (DSSC) Using Anodic Titanium Oxide (ATO) Nanotube Arrays, J. Electrochem. Soc. 156 (2009) C304–C312.